JOURNAL OF SOLID STATE CHEMISTRY 111, 238–246 (1994)

$Eu_{2.5}Ba_{2.5}Co_2Cu_3O_{12}$, an Intergrowth of the "112" and "123" Structures

L. Barbey, B. Domengès, N. Nguyen, and B. Raveau

Laboratoire CRISMAT-ISMRA/Université de Caen CNRS URA1318, Bd du Maréchal Juin, 14050 Caen Cedex, France

Received July 14, 1993; accepted September 21, 1993

A regular intergrowth of the 112 and 123 structures has been synthesized for the first time. The new phase $Eu_{2.5}Ba_{2.5}Co_2Cu_3O_{12}$ crystallizes in the space group $P4/mmm$ with $a = 3.8935(2)$ Å and $c = 19.085(2)$ Å. Its XRPD and HREM study demonstrates that it corresponds to the first ($n = n' = 1$) member of the intergrowth series $[LnBa(Co,Cu)_2O_5]_n\,[LnBa_2(Co,Cu)_3O_7]_{n'}$. The observation of several intergrowth defects suggests that it should be possible to synthesize other members of the series. The EDX analysis and the HREM observations show a complex cationic distribution involving local orderings of cobalt and copper that may mainly occur on the intermediate (Cu,Co) sites, i.e., between the pyramidal layers.

INTRODUCTION

Recent studies of the layered cuprates have shown close relationship between the 92 K superconductor $YBa_2Cu_3O_7$ called **123** (1, 2) and the iron substituted phase $YBaCuFeO_5$ (3), called **112**. In both structures (Fig. 1), one observes double layers of $Cu(Fe)O_5$ pyramids interleaved with yttrium cations; in the **123** cuprate, the pyramidal layers are interconnected through rows of CuO_4 square planar groups, whereas in the **112** phase they share their apical oxygens forming double pyramidal layers. Thus, the $[CuFeO_5]_\infty$ framework can be deduced from the $[Cu_3O_7]_\infty$ lattice by just eliminating rows of CuO_4 groups and connecting the pyramidal layers. This bidimensional similarity between the two structures suggests that it should be possible to generate ordered intergrowths, considering the fact that the **112** structure requires the presence of iron (3) or of cobalt (4, 5) to be stabilized. Moreover, such materials are likely to exhibit original magnetic properties, as recently shown for the **112** cobalt substituted phase $YBaCo_{2-x}Cu_xO_5$ with x ranging from 0.3 to 1 (6). The present work deals with the synthesis and crystal structure of the cobalt-cuprate $Eu_{2.5}Ba_{2.5}Co_2Cu_3O_{12}$, the first member of the intergrowth series $[LnBa(Co,Cu)_2O_5]_n\,[LnBa_2(Co,Cu)_3O_7]_{n'}$.

EXPERIMENTAL

The different compositions of the system Eu–Ba–Co–Cu–O were explored from adequate mixtures of Eu_2O_3, BaO_2, CuO, Co_3O_4, and cobalt according to the nominal formula $Ba_{3-x}Eu_{2+x}Cu_{5-y}Co_yO_{12}$ in order to try to synthesize the first member of the intergrowth series. The oxides were intimately ground in an agate mortar, pressed in the form of bars, and placed in air sealed silica tubes. Different thermal treatments were tested, and the best results were obtained by heating the sample first at 800°C for 24 hr and then at 980°C for 6 days.

The powder X-ray diffraction pattern was registered by step scanning over an angular range of $15° < 2\theta < 90°$ with an increment of 0.02° (2θ) by means of a Philips diffractometer using the CuK_α radiation. Lattice constants were refined and structural calculation were performed using the profile analysis program DBW 3.2 (7). For the electron microscopy, the sample was gently ground in *n*-butanol and deposited on a holey carbon coated aluminum grid. Electron diffraction (ED) was performed on a JEM 200CX equipped with a tilting (±60°) rotating goniometer, and high resolution was performed on a TOPCON2B equipped with a double tilt ±10° goniometer and an objective lens with a spherical aberration constant $C_s = 0.4$ mm. Image calculations were performed according to the multislice method of the EMS program (8). The determination of the oxygen content was carried out by microthermogravimetric analysis by reducing the sample in an argon–hydrogen atmosphere (10% H_2) from 20 to 980°C.

RESULTS AND DISCUSSION

Structure

For the above experimental conditions, the powder X-ray diffraction analysis showed that the best results were obtained for the nominal composition $Eu_{2.5}Ba_{2.5}Co_2Cu_3O_{12}$. The X-ray diffractogram corresponding to this

0022-4596/94 $6.00

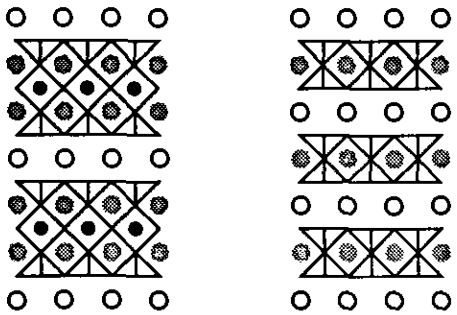

FIG. 1. Projection of idealized **123** and **112** structures.

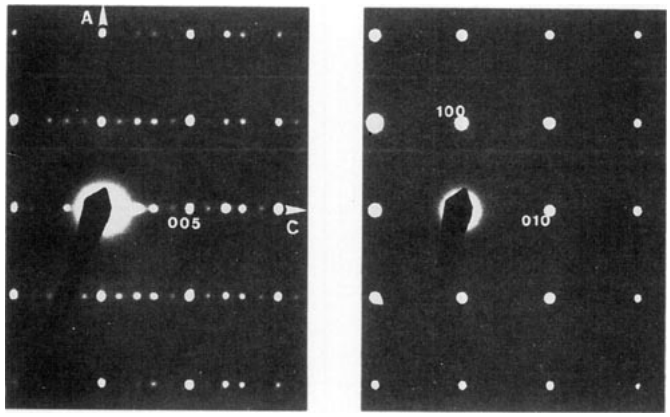

FIG. 3. [010] and [001] E.D. patterns showing no reflection existence condition (*P4/mmm* space group) and the relation of the **c** parameter with the a_p subcell: $c \approx 5\ a_p$.

composition (Fig. 2) shows that it is monophasic and typically related to the perovskite structure, but that it can be indexed either in a **123**- or in a **112**-type cell (except for one extra reflection on the Guinier film characteristic of a large parameter, d = 19.1 Å). The ED patterns of this phase (Fig. 3) confirm the superstructure with respect to the perovskite subcell (a_p) leading to the space group *P4/mmm* with $a \approx a_p$ and $c \approx 5a_p$. The powder X-ray diffractogram of this phase is then indexed on this basis in a tetragonal cell with a = 3.8935(2) Å and c = 19.085(2) Å.

The value of the **c** parameter, corresponding to the sum "$c_{123} + c_{112}$," suggests that this phase corresponds to the single intergrowth of one **123** layer with one **112** layer according to the structural model proposed in Fig. 4. This hypothesis is strongly supported by our HREM investigation, as shown from the ⟨100⟩ image of this phase (Fig. 5), for a focus value close to 10 nm, where the cations of the structure are highlighted. One observes, by analogy with the **123** structure contrast, rows of brighter dots parallel to ⟨100⟩ that are associated to the copper atoms of the intermediate layer (i.e., square planes) in the **123** structure. Between the latter, nine rows of 0.38-nm spaced dots alternate, which can be interpreted by the sequence Ba–Cu–Eu–Cu–Ba–Cu–Eu–Cu–Ba along **c**. This cationic lattice is thus compatible with the layer stacking:

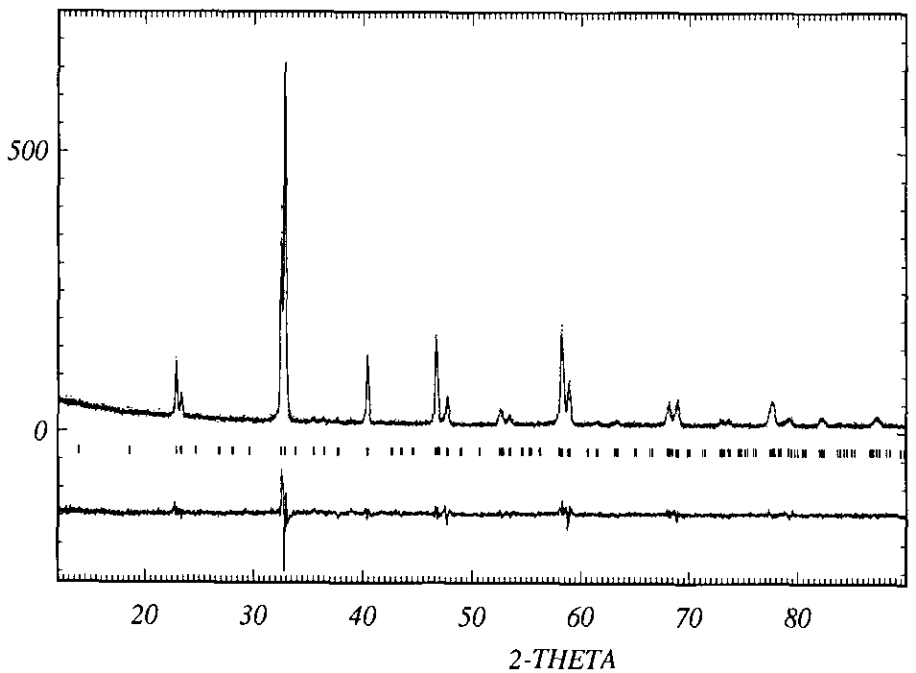

FIG. 2. Observed, calculated, and difference X-ray powder diffractogram of the $Eu_{2.5}Ba_{2.5}Co_2Cu_3O_{12}$ compound.

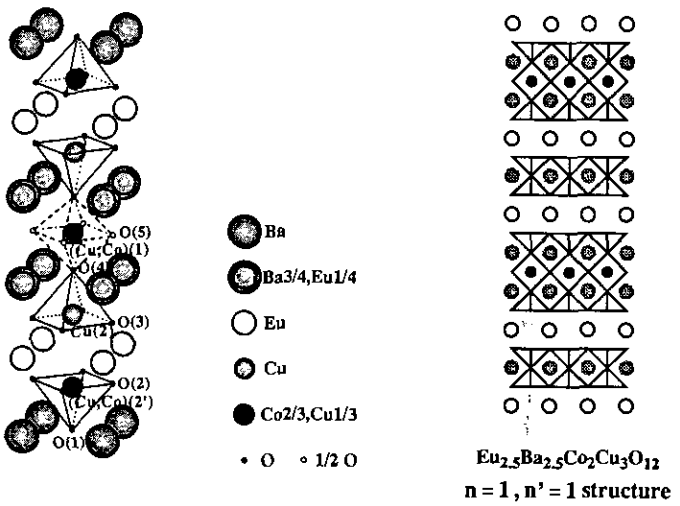

FIG. 4. $Eu_{2.5}Ba_{2.5}Co_2Cu_3O_{12}$ structure: perspective view and idealized projection.

$CuO-BaO-CuO_2-Eu-CuO_2-BaO-CuO_2-Eu-CuO_2-BaO-CuO$. In fact, the EDS analysis performed on 23 microcrystals of the oxide of nominal composition $Eu_{2.5}Ba_{2.5}Co_2Cu_3O_{12}$ shows that the cationic distribution is not homogeneous but varies significantly from one crystal to the other, especially for Ba and Eu according to the formula $Eu_{2.1-2.7}Ba_{2.3-2.9}Co_{1.9-2.2}Cu_{2.8-3.1}$. Nevertheless, in order to check this model on the basis of image simulations, structure resolution was performed from powder X-ray data. The starting atomic positions were deduced from those of the **123** and **112** structures. Considering the low sensitivity of X rays to light atoms compared to heavy ones, the *B* factors of oxygen were fixed to 1 $Å^2$. In the same way, the occupancy factors of the metallic, i.e., mixed Ba–Eu and Co–Cu sites could not be refined due to the close scattering factors of these elements. Based on $YBa_2(Cu,Co)_3O_7$ studies (9), it was supposed that Co was equally substituted on Cu(1) and Cu(2′) sites; i.e., the intermediate Cu site of the **123** layer and the pyramidal Cu site of the **112** layer. Positional parameters for all

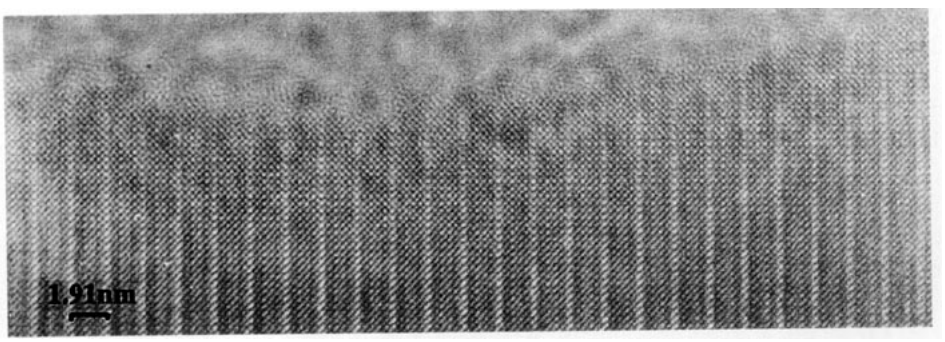

FIG. 5. Typical ⟨100⟩ HREM image of $Eu_{2.5}Ba_{2.5}Co_2Cu_3O_{12}$ microcrystals; the focus value is close to 10 nm.

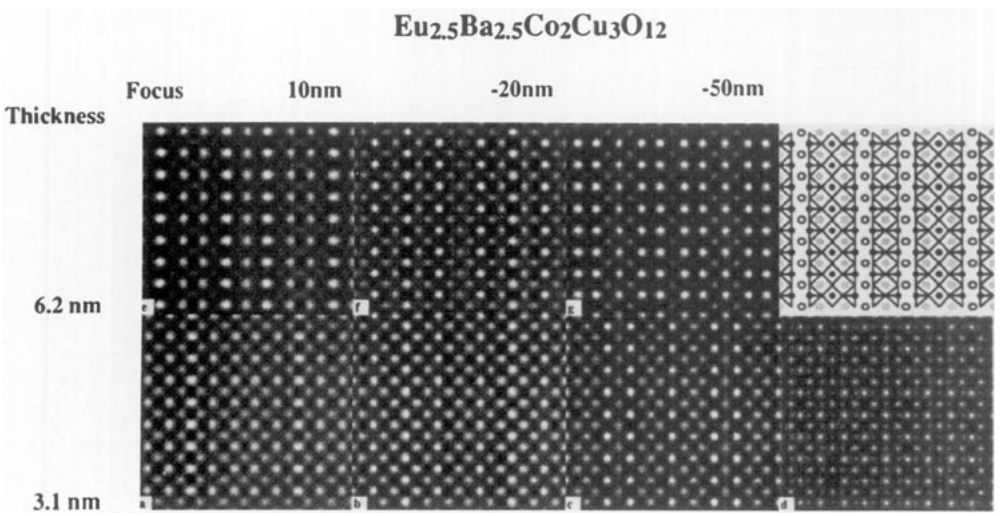

FIG. 6. Characteristic images of calculated through focus series for two different thicknesses. Calculation parameters are: voltage V = 200 kV, spherical aberration constant C_s = 0.4 mm, focus spread Δ = 10 nm, half-angle convergence α = 0.8 mrad, objective aperture diameter 14 nm^{-1}. Projected potential is in (d).

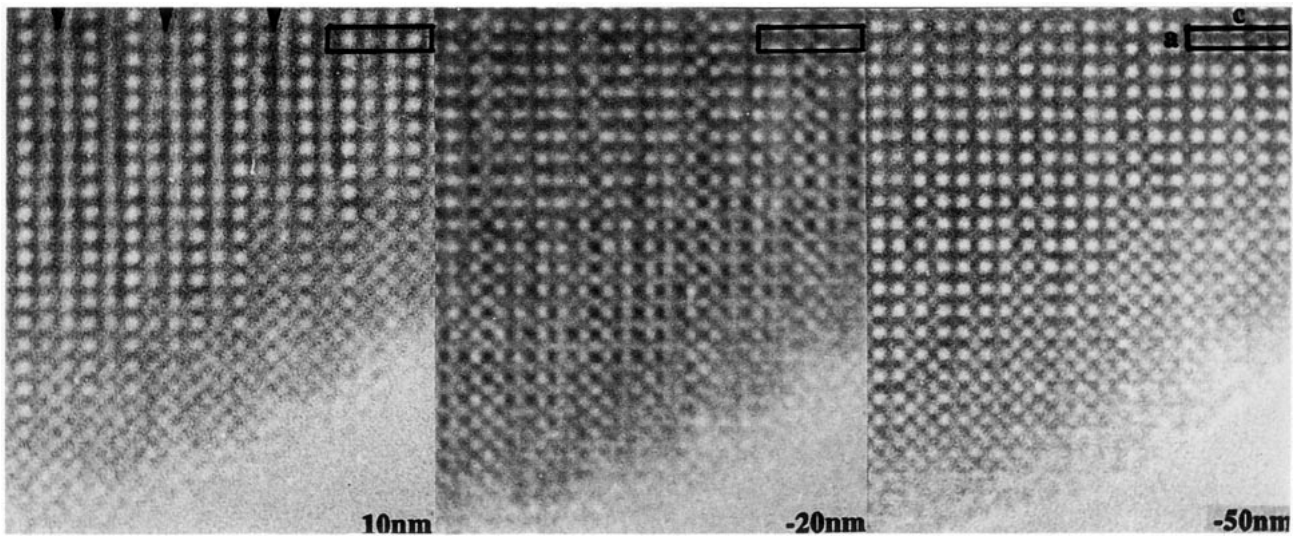

FIG. 7. Characteristic images of experimental through focus series. Note darker contrast at the (Cu,Co) layer level (arrowed) on the 10 nm image.

atoms and isotropic thermal factors were successively refined, leading to the following values of the agreement factors: $R_p = 0.098$, $R_{wp} = 0.125$, and $R_i = 0.076$. The refined parameters (Table 1), if they are not accurate for the oxygen atoms, are significant for the metallic atoms and confirm the stacking sequence proposed for the HREM image. Taking into consideration the size of the cations and the TGA results that led to an oxygen content of 11.87(5) per formula, the distribution of the cationic species in the **123** and **112** layers can be represented by

TABLE 1
$Eu_2Ba_3Co_2Cu_3O_{12}$: Structural Parameters

Atom	Site	x	y	z	B(Å)^2
Eu	2*g*	0.5	0.5	0.1996(6)	0.2(2)
Ba	1*a*	0.5	0.5	0	0.2(4)
$Eu_{1/4}Ba_{3/4}$	2*g*	0.5	0.5	0.3892(3)	0.8(3)
$(Cu_{1/3}Co_{2/3})(1)$	1*d*	0	0	0.5	1[a]
Cu(2)	2*h*	0	0	0.2934(9)	1[a]
$(Cu_{1/3}Co_{2/3})(2')$	2*h*	0	0	0.1077(8)	0.1(3)
O(1)	1*c*	0	0	0	1
O(2)	4*i*	0.5	0	0.122[b]	1
O(3)	4*i*	0.5	0	0.277[b]	1
O(4)	2*h*	0	0	0.407[b]	1
O(5)[c]	2*e*	0.5	0	0.5	1

Note. $a = 3.8935(2)$ Å, $c = 19.085(2)$ Å; S. G. is *P4/mmm*. $R_p = 9.8\%$, $R_{wp} = 12.4\%$, $X^2 = 2.34$, $R_i = 7.2\%$, $U = 0.1996$, $V = -0.0612$, $W = 0.0365$.

[a] B parameters were fixed to 1 Å^2, as they could not be refined.

[b] z_0 parameters were refined and then fixed to a value leading to appropriate cation–oxygen distances.

[c] In agreement with O_{12} stoichiometry and tetragonal symmetry, O(5) occupancy is fixed to 0.5.

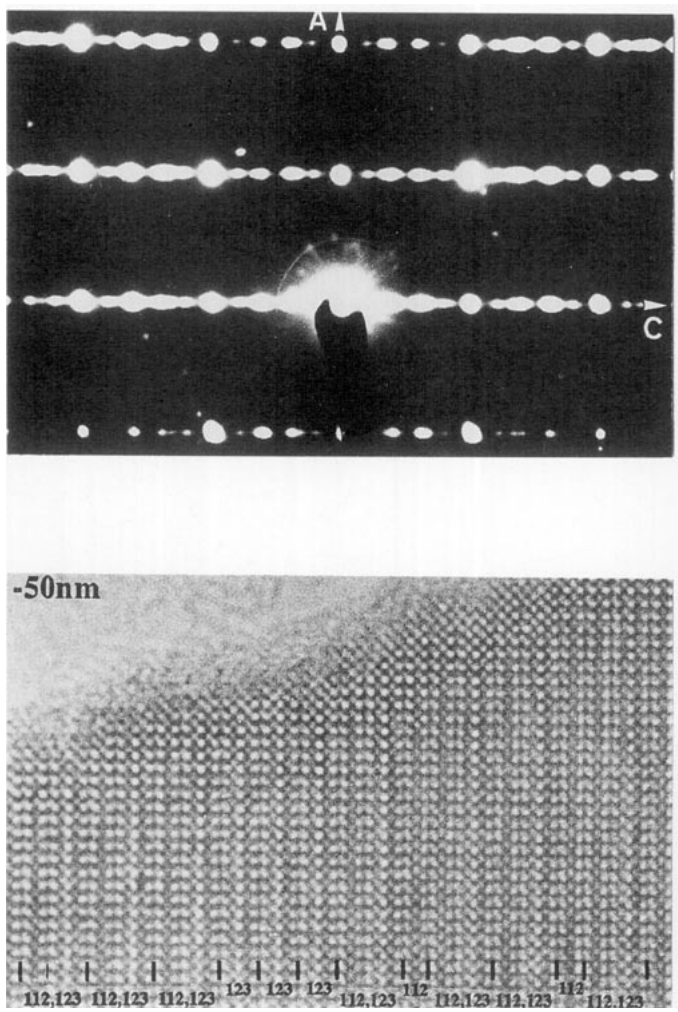

FIG. 8. ⟨100⟩ E.D. pattern and corresponding HREM image of a microcrystal showing disordered **112–123** layer stacking.

the formula $[Eu(Ba_{3/4}Eu_{1/4})_2(Cu,Co)_3O_7]$[123] $[EuBa(Co,Cu)_2O_5]$[112].

In order to verify our previous interpretation of the HREM contrast, ⟨100⟩ image calculations were performed based on the XRD results. Characteristic images of the calculated through focus series are shown in Fig. 6 for two different thicknesses. For a 3.1-nm-thick crystal, the three selected images are based on an almost square array (0.27 nm^2 of bright dots), among which some appear brighter depending on the focus value. At 10 nm focus, the dots are related to the cations of the structure, and the 0.39-nm-spaced brighter dots forming rows parallel to **a** correspond to the mixed (Co,Cu)(1) site of the **123**-type slab, so that between these rows, nine rows of dots are counted in agreement with the sequence (Cu,Co)(1)–(Ba,Eu) – Cu(2) – Eu – (Co,Cu)(2′) – Ba – (Co,Cu)(2′) – Eu–Cu(2)–(Ba,Eu)–(Cu,Co)(1); at −20 nm focus, the low electron density zones are highlighted and the 0.39-nm-spaced, slightly brighter dots forming rows parallel to **a** correspond to oxygen vacancies at the Eu level so that one can count between these brighter rows five rows of dots for the **123**-type slabs corresponding to –O(3)–O(4)–O(5)–O(4)–O(3)– and three rows for the **112**-type slabs corresponding to –O(2)–O(1)–O(2)–; at −50 nm focus, high electron density zones are highlighted and the 0.39-nm-spaced, brighter dots forming rows correspond to barium so that they form pairs of rows in the **123**-type layer and isolated rows in the **112**-type layer: between these, the rows of grayer dots are easily associated to other rows of cations of the structure. Calculations

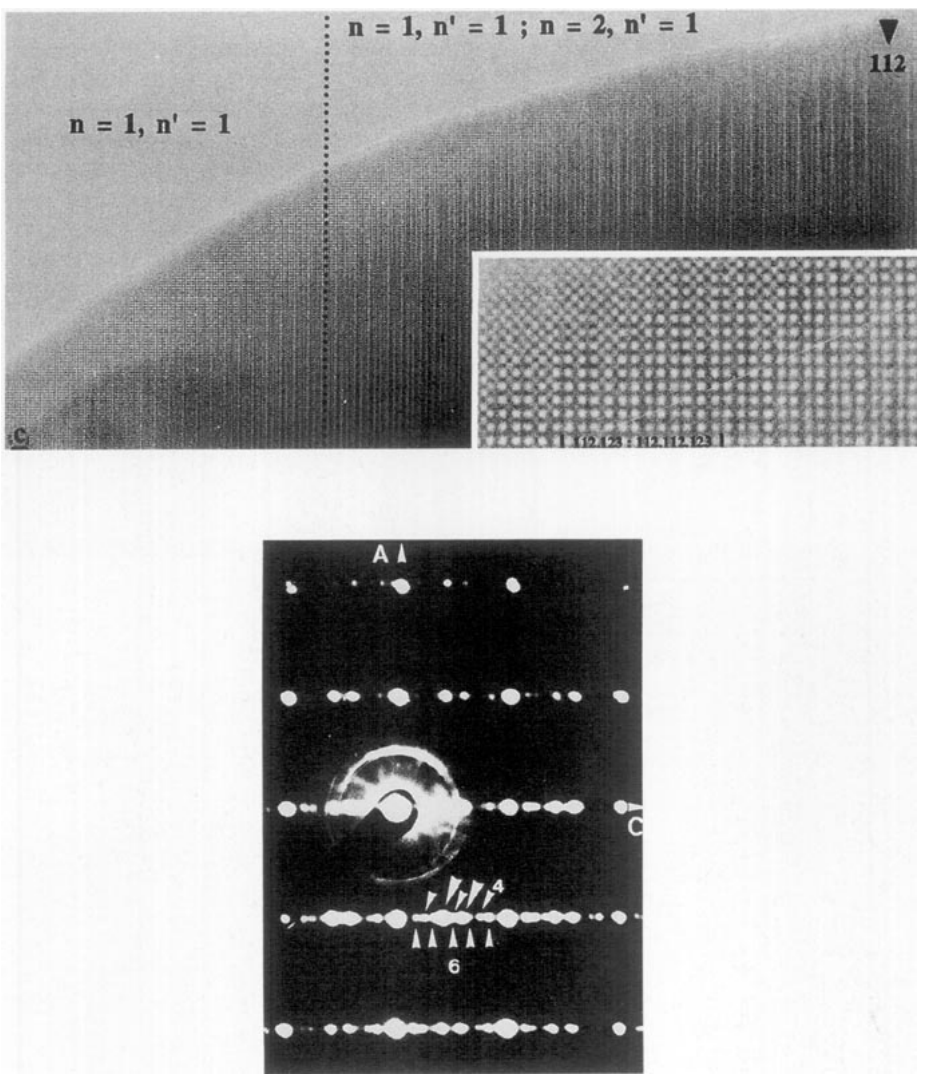

FIG. 9. ⟨100⟩ HREM image and corresponding E.D. pattern of a microcrystal showing beside the (1,1) matrix a domain characterized by a new ordered intergrowth sequence: [(1,1); (2,1)]. Note also a small **112**-type domain (arrowed). Along **c** on the E.D. pattern, three sets of dots can be distinguished corresponding to $6a_p$ and $4a_p$ (small arrows) and $5a_p$ (only the two strongest are marked with big arrows) periodicities.

have been performed for thicker crystals to determine the focus value which will allow easy imaging of **112** and **123** slabs, and thus allow the detection of any intergrowth defect. For a 6.2 nm thickness, 10 nm and −50 nm focus images highlight the layer stacking. At 10 nm focus, the higher electron density zones are highlighted so that the rows of 0.39-nm-spaced, brighter dot parallel to **a** correspond to the Eu layer, whereas between them, the rows of 0.39-nm-spaced, slightly less bright dots correspond to the Ba and (Ba,Eu) layers (two rows in the **123**-type slab and one in the **112**-type); the very small gray dots are related to the (Co,Cu) sites of the structure. At −50 nm focus, the 0.39-nm, brighter dots correspond to the (Co,Cu) atoms, so that, considering the interlayer (Cu,Co) distances, the groups of two rows parallel to **a** are related to the *(Cu,Co)(2)* and *(Cu,Co)(2′)* atoms of the facing square pyramids of the **123** and **112** layers, respectively, whereas the isolated ones correspond to the (Co,Cu)(1) atoms of the intermediate layer in the **123**-type slab. The periodicity of the (Cu,Co) layers is thus described by the sequence S.R.–D.R.–D.R.–S.R. of single rows (S.R.) and

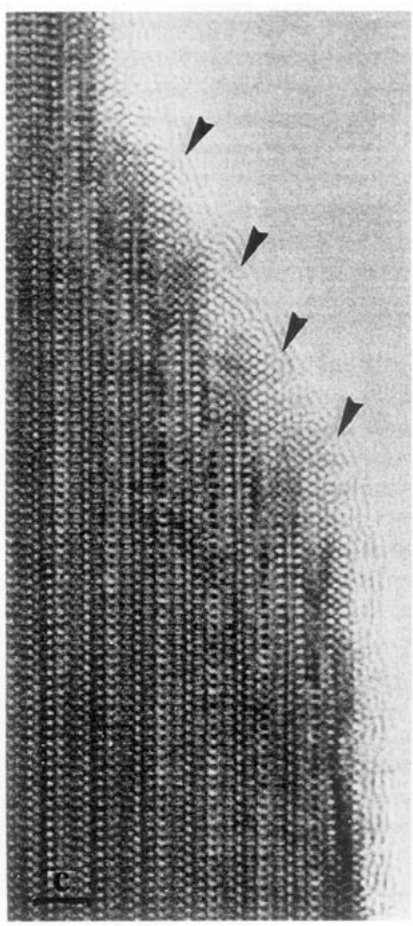

FIG. 10. ⟨100⟩ HREM image of a microcrystal showing on the edge EuO_2 fluorite-type stackings (arrowed).

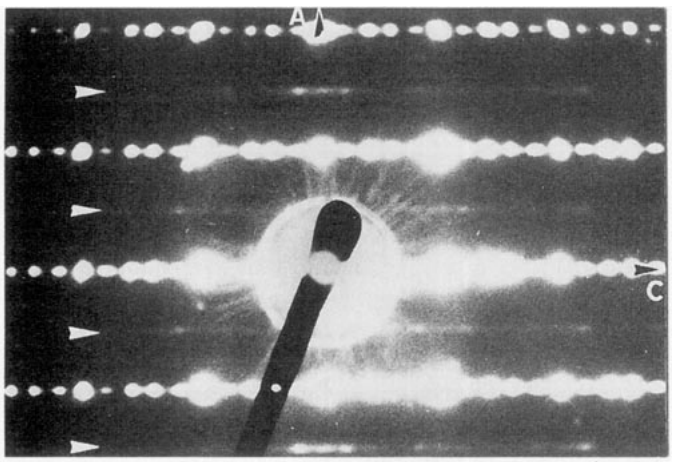

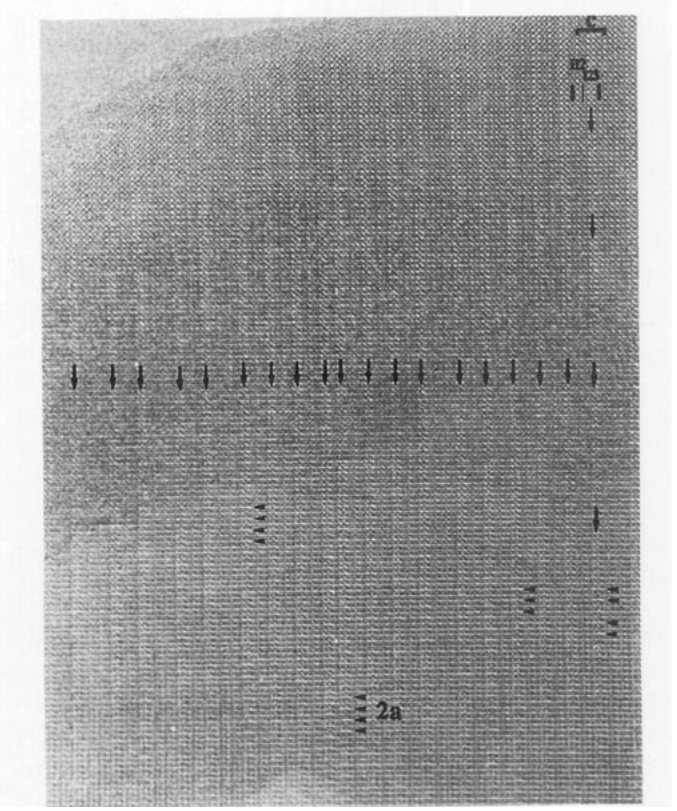

FIG. 11. ⟨100⟩ E.D. pattern showing diffuse streaks parallel to **c** which involve a doubling of the **a** parameter (arrowed). On the corresponding HREM image, a modulation of contrast is observed (small arrows on lower side) at the **123**-type slab level (arrowed).

double rows (D.R.), whereas the grayer dots correspond to other cations of the structure. This image will appear very useful in the identification of the layer stacking; at −20 nm focus, low electron density zones are highlighted, and the stacking sequence does not image so obviously.

The experimental images taken for the three discussed focus values (Fig. 7) show that the observed contrast fits pretty well with the calculated ones, and direct interpretation of the contrast for thicker zones appears obvious indeed. A careful examination of the +10 nm image shows a darker contrast between the bright dot rows—i.e., Eu and Ba layers—which as a consequence move apart from each other. This variation of the contrast, which occurs at the level of the (Co,Cu) layers, may be related to the substitution of Co for Cu and the variation of atomic environment it may induce.

Thus, this detailed investigation definitely demonstrates that the phase $Eu_{2.5}Ba_{2.5}Co_2Cu_3O_{12}$ corresponds to the regular stacking of **123** and **112** layers (Fig. 4) and can be described as the member $n = n' = 1$ of the intergrowth series $[EuBa(Co,Cu)_2O_5]_n\,[EuBa_2(Co,Cu)_3O_7]_{n'}$.

Defects

Besides the numerous crystals showing a regular and neat contrast, some are characterized by defective areas, due either to intergrowth or to order–disorder phenomena.

Intergrowth defects. The existence of intergrowth defects, corresponding to the local formation of other $[n, n']$ members of the series, could be expected in agreement with the observations previously made for $YBa_2Cu_2CoO_7$ and $YBaCuCoO_5$ (5). The ED pattern of some crystals confirms the existence of such defects. Streaks parallel to **c** on the ⟨100⟩ ED pattern are related to disordered layer stackings (Fig. 8.) Moreover, the elongation of strong spots corresponding to the periodicity c_{112} and c_{123} suggests a disorder in the stacking of **112**- and **123**-type slabs. Indeed, the corresponding image confirms this idea and the following sequence is observed: **(112,123)$_3$ – (123)$_3$ – (112,123) – 112 – (112,123)$_2$ – 112 – (112,123).** Different stackings of the **112** and **123** layers can appear as microdomains in the (1,1) matrix. An example is shown in Fig. 9, in which the sequence **112–123–112–112–123** corresponds to the intergrowth of the member (1,1) with the member (2,1). The resulting ED pattern is rather complex (Fig. 9). Along **c**, it can be decomposed as the superposition of three types of superstructures referred to a_p as "$5a_p$," "$6a_p$," and "$4a_p$," corresponding to the (1,1) domain, the half periodicity of [(1,1);(2,1)] intergrowth, and the "**112–112**" subsequence, respectively. A small domain involving six **112**-type slabs is also observed.

The possibility of intergrowing these structures with the fluorite structure by replacing the single fluorite layers at the level of europium with larger fluorite-type layers is observed on some crystal edges (Fig. 10) similarly to the previous studies of the oxide $BaNdCe_{0.9}Fe_{1+x}Cu_{1-x}O_{7-\delta}$ (10).

Modulation of the contrast: local orderings. Some ⟨100⟩ ED patterns exhibit weak streaks parallel to **c**, involving a doubling of the **a** parameter (Fig. 11). The corresponding HREM image shows on a thick part of the crystal a modulation of the contrast in agreement with the doubling of the **a** parameter. This modulation appears at the **123**-type

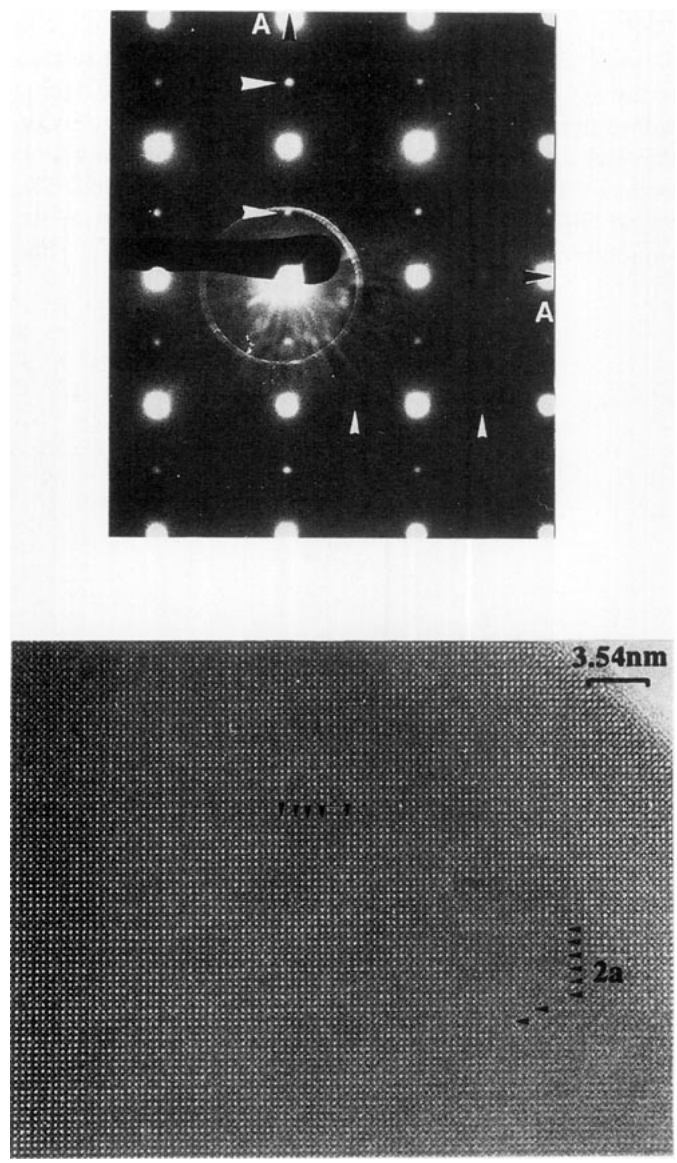

FIG. 12. [001] E.D. pattern showing extra dots which involve the doubling of the **a** parameter in a 90°-oriented way. The corresponding HREM image shows that the modulation of contrast is widely established along one **a** direction and very locally along the perpendicular one.

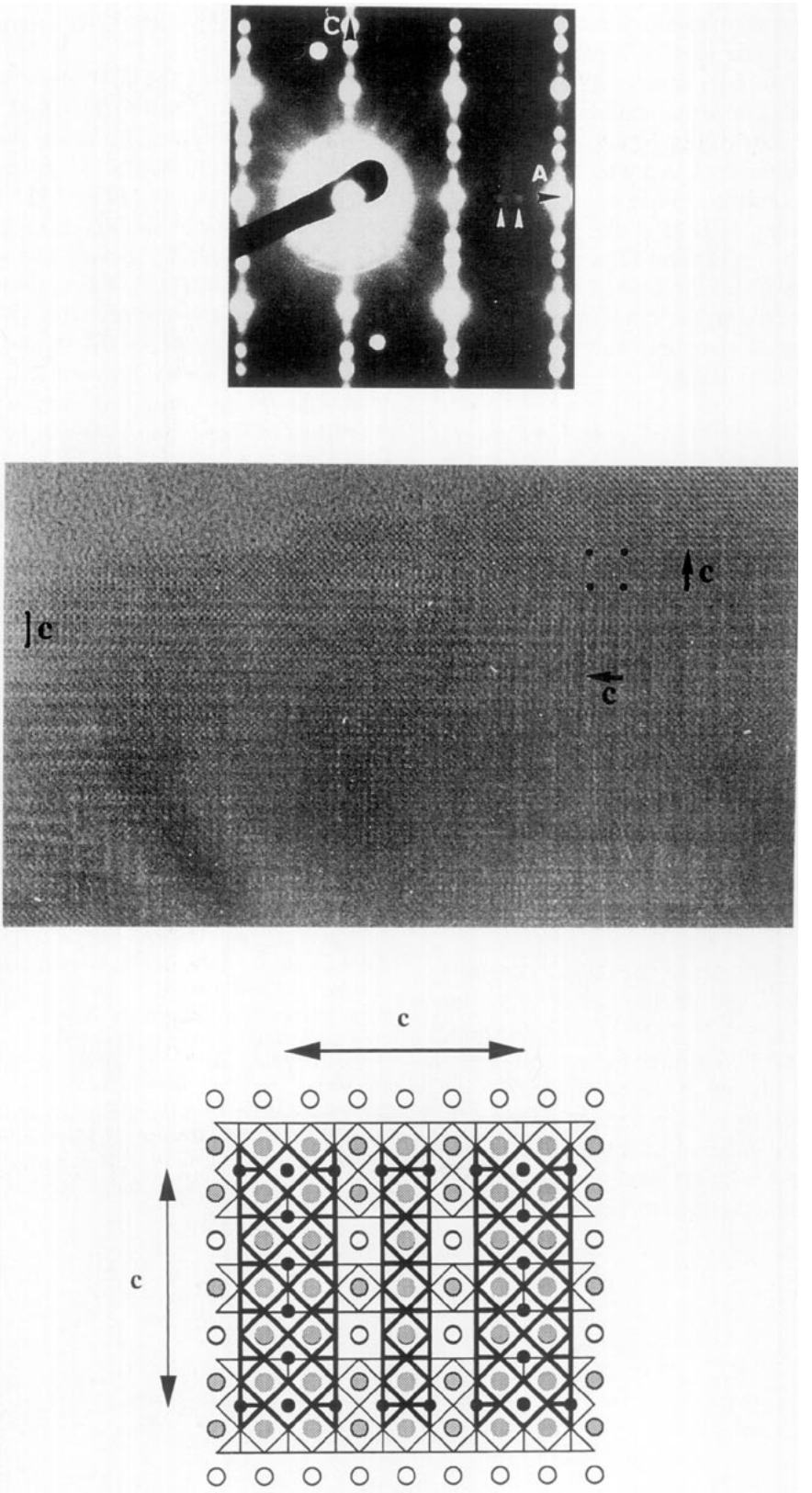

FIG. 13. ⟨100⟩ E.D. pattern showing weak extra dots related to 90°-oriented **c** axes. The corresponding HREM image shows a contrast resulting from the superimposition of two 90°-oriented domains as proposed on the schematic model.

slab level. Similar observations were made with the electron beam parallel to **c**. The [001] ED pattern (Fig. 12) clearly shows weak extra dots (arrowed) which double one parameter, but a careful examination allows one to distinguish very weak extra dots (small arrows) which double the other parameter in such a way that the superstructure must have taken place in two 90°-oriented domains. The corresponding HREM image shows one of the classical [001] contrasts (**112** and **123** structures), i.e., a square 0.38-nm^2 array of bright dots. A modulation of the contrast, corresponding to the doubling of one **a** parameter, is observed on a large area, whereas tiny zones show the same modulation established along the perpendicular direction.

These observations do not allow the determination of the accurate supercell since no reconstruction of the reciprocal space could be performed on such crystals. Nevertheless, they clearly indicate that a local ordering takes place at the level of the **123** slabs. It may be related to the ordering of Co and Cu in the **123** layers, but also to the ordering of Eu and Ba atoms on the barium sites. Although it is not realistic to propose a model at this stage of the observations, it appears most likely that such a disturbance of the contrast cannot be due to a single ordering of the atoms, but to a significant change of the geometry of their coordination. Consequently, it is most probable that the local ordering of cobalt and copper at the level of the (Cu, Co) (1) sites is at the origin of this phenomenon, since cobalt will exhibit at this level either a tetragonal or a pyramidal coordination as in Co-substituted **123** compounds (9), whereas copper will exhibit mainly the square planar coordination.

Oriented domains. Very rarely, the ⟨100⟩ ED patterns show weak spots besides the intense set of reflections characteristics of the structure (Fig. 13). This corresponds to 90°-oriented domains, as confirmed by the corresponding HREM image that shows the superimposition of a small 90°-rotated domain to a large regular matrix. This observation can easily be understood if one considers the stacking of two successive layers along **a** that exhibit a 90°-oriented *c*-axis as schematized in Fig. 13.

CONCLUDING REMARKS

The synthesis of the first member of the intergrowth series $[Ln, Ba(Co, Cu)_2O_5]_n$ $[LnBa_2(Co, Cu)_3O_7]_{n'}$ has been made for the first time. This opens the road to the exploration of the other members corresponding to the intergrowth between the **112** and **123** structures, as shown from the existence of various extented defects. The distribution of the cationic species is so far not understood, but there is no doubt that orderings take place at least between cobalt and copper sites. Such phenomena may play an important role for the stabilization of the different members of the series, and consequently, thermal treatments should be optimized. The study of the magnetic properties of these materials will be investigated.

REFERENCES

1. M. K. Wu, J. R. Ashburn, C. J. Torng, P. H. Hor, R. L. Meng, L. Gao, Z. J. Huang, Y. Z. Wang, and C. W. Chu, *Phys. Rev. Lett.* **58,** 908 (1987).
2. Y. Lepage, W. R. McKinnon, J. M. Tarascon, L. H. Greene, G. W. Hull, and D. M. Hwang, *Phys. Rev. B* **35,** 7245 (1987); R. J. Cava, B. Battlog, R. B. Vandover, D. N. Murphy, S. Sunshine, T. Siegrist, J. P. Remeika, E. A. Rietman, S. Zahurak, and G. P. Espinosa, *Phys. Rev. Lett.* **58,** 1676 (1987); J. J. Caponi, C. Chaillout, A. W. Hewat, P. Lejay, N. Nguyen, B. Raveau, J. L. Soubeyroux, J. L. Tholence, and R. Tournier, *Europhys. Lett.* **12,** 1301 (1987); and M. A. Beno, L. Soderhölm, D. W. Capone, D. Hinks, J. O. Jorgensen, I. K. Schuller, C. U. Segre, K. Zang, and J. D. Grace, *Appl. Phys. Lett.* **51,** 57 (1987).
3. L. Er-rakho, C. Michel, Ph. Lacorre, and B. Raveau, *J. Solid State Chem.* **73,** 531 (1988).
4. L. Barbey, N. Nguyen, V. Caignaert, M. Hervieu, and B. Raveau, *Mater. Res. Bull.* **27,** 295 (1992).
5. M. Jacob, S. Hansen, and S. Sturefelt, *Microsc. Microanal. Microstruct.* **1,** 319 (1990).
6. L. Barbey, V. Caignaert, N. Nguyen, F. Studer, and B. Raveau, *J. Solid State Chem.*, in press (1994).
7. D. B. Wiles and R. A. Young, *J. Appl. Crystallogr.* **14,** 149 (1981).
8. P. A. Stadelmann, *Ultramicroscopy* **14,** 149 (1981).
9. H. Renevier, J. J. Hodeau, M. Marezio, A. Fontaine, A. Michalowicz, and G. Touillon, *Phys. Rev. B* **47,** 11398 (1993).
10. C. Michel, M. Hervieu, and B. Raveau, *J. Solid State Chem.* **92,** 339 (1991).